Lawrence Berkeley National Laboratory

Title
Molecular anisotropy effects in carbon K-edge scattering: depolarized diffuse scattering and optical anisotropy

Permalink
https://escholarship.org/uc/item/4698r1g7

Author
Stone, Kevin H.

Publication Date
2014-09-14

Molecular anisotropy effects in carbon *K*-edge scattering: Depolarized diffuse scattering and optical anisotropy

Kevin H. Stone[†] and Jeffrey B. Kortright

Materials Sciences Division, Lawrence Berkeley National Laboratory, 1 Cyclotron Road,
Berkeley, California 94720, USA
[†]*Current address, Stanford Synchrotron Radiation Laboratory, SLAC National Accelerator*
Laboratory, 2575 Sand Hill Road, Menlo Park, California, 94025, USA

ABSTRACT

Some polymer properties, such as conductivity, are very sensitive to short- and intermediate-range orientational and positional ordering of anisotropic molecular functional groups, and yet means to characterize orientational order in disordered systems are very limited. We demonstrate that resonant scattering at the carbon *K*-edge is uniquely sensitive to short-range orientation correlations in polymers through depolarized scattering at high momentum transfers, using atactic polystyrene as a well-characterized test system. Depolarized scattering is found to coexist with unpolarized fluorescence, and to exhibit pronounced anisotropy. We also quantify the spatially averaged optical anisotropy from low-angle reflectivity measurements, finding anisotropy consistent with prior visible, x-ray absorption, and theoretical studies. The average anisotropy is much smaller than that in the depolarized scattering and the two have different character. Both measurements exhibit clear spectral signatures from the phenyl rings and the polyethylene-like backbone. Discussion focuses on analysis considerations and prospects for using this depolarized scattering for studies of disorder in soft condensed matter.

1

Disclaimer

This document was prepared as an account of work sponsored by the United States Government. While this document is believed to contain correct information, neither the United States Government nor any agency thereof, nor the Regents of the University of California, nor any of their employees, makes any warranty, express or implied, or assumes any legal responsibility for the accuracy, completeness, or usefulness of any information, apparatus, product, or process disclosed, or represents that its use would not infringe privately owned rights. Reference herein to any specific commercial product, process, or service by its trade name, trademark, manufacturer, or otherwise, does not necessarily constitute or imply its endorsement, recommendation, or favoring by the United States Government or any agency thereof, or the Regents of the University of California. The views and opinions of authors expressed herein do not necessarily state or reflect those of the United States Government or any agency thereof or the Regents of the University of California.

I. INTRODUCTION

Properties of polymers and soft condensed matter can be strongly influenced by inherent structural disorder ranging over length scales from molecular functional groups to characteristic conformation and crystallization scales up to sample dimensions. Charge transport in organic electronics, for example, is sensitive to such short- and intermediate-range disorder, whether it be along π-stacking directions or conjugated chains. Structural disorder is often characterized via scattering methods and modeled in terms of positional pair-correlation functions. Molecular functional groups are generally anisotropic, however, and disorder in their relative orientation influences conductivity and can be distinguished from disorder in their position. Furthermore, orientation correlations generally evolve differently with distance than do positional correlations, and hence they will have different Fourier spectra. Typical scattering probes of disordered polymer structure (hard x-rays, neutrons, electrons) are not directly sensitive to orientation correlations of organic groups at important 1 - 100 *nm* length scales.

Resonant electromagnetic interactions are sensitive to the orientation of anisotropic scattering entities through polarization effects arising from off-diagonal scattering terms. In the visible spectral regime interactions are generally resonant, giving rise to depolarized scattering, optical activity in liquid crystals, circular dichroism, and many other examples in which molecular anisotropy is sensed [1-4]. Hard x-ray scattering typically results from the non-resonant, isotropic (Thompson) part of the atomic scattering factor and so does not sense molecular orientation directly. Resonant effects at core levels of heavy species in molecular crystals [5-7] and at the sulfur *K*-edge in liquid crystals [8] sense molecular anisotropy more directly, activating otherwise forbidden reflections. Considering that x-ray absorption spectroscopy (XAS) at the carbon *K*-edge ($\sim$290 eV, $\lambda \ \Box \ 4.4 \ nm$) senses strong anisotropy in

oriented molecules [9-13], resonant scattering at the carbon edge [14, 15] is also expected to sense molecular anisotropy in polymers, although most early applications have assumed isotropic scattering properties. Exceptions include laterally averaging specular reflectivity measurements of large resonant birefringence in graphite [16] and optical anisotropy in liquid crystal polymer [17] and self-assembled monolayer [18] films. By extension, resonant depolarized (off-diagonal) scattering should result from orientation fluctuations of functional groups at length scales at least as short as $\lambda/2 = 2.2$ *nm*, and thus provide a probe of orientational texture in the mesoscale spatial frequency range that is currently unavailable.

Herein we report resonant depolarized resonant scattering from short-range anisotropy fluctuations in polymers. We chose to explore resonant anisotropy effects in atactic polystyrene (aPS) for several reasons. It is a disordered (amorphous) polymer containing 2 functional groups; highly anisotropic, rigid phenyl rings attached to the flexible polyethylene-like chain backbone as shown for a single monomer in Figure 1. The visible optical properties of aPS are well documented [19-22], as is its hard x-ray scattering in small-angle [23-26], wide-angle [23, 27-29], and surface sensitive [30-32] regimes. Spatially averaged anisotropy in C *K*-edge XAS has also been reported [12, 13]. These experimental studies agree with theoretical models, making it a well-characterized system with non-trivial and unexplored resonant anisotropy behavior expected in diffuse scattering. Orientation fluctuations of phenyl groups and backbone segments scatter at relatively short chain conformation length scales corresponding to *q* values accessible at the carbon edge and below well-known amorphous charge-scattering peaks. Finally, while the expectation of depolarized scattering from orientation fluctuations was clear at the outset, it was not obvious that it would be observable for reasons discussed below.

Following discussion of samples and measurement considerations, we present results first from low-angle specular reflectivity and then from high-angle diffuse scattering measured with incident *s*- and *p*-polarization. We find molecular anisotropy effects in spatially averaging reflectivity in general agreement with previous studies, and in depolarized diffuse scattering from short-range orientation fluctuations.   In each measurement, contributions are found to originate from both the phenyl rings and the chain backbone. Discussion throughout centers on analytical considerations involved in the measurements and their interpretation in light of previous studies, and concludes with considerations regarding the utility of the newly observed resonant depolarized scattering in studies of soft condensed matter.

II. MATERIALS AND METHODS

A. Atactic polystyrene film samples

We investigate dried, toluene solvent cast films of atactic polystyrene as both thick, drop-cast and ultrathin, spin-cast films of several molecular weights summarized in Table 1. This range of samples ensures that the observed trends are general and facilitates comparison with previous studies. Thick films ($t \cong 2$ μm) were drop-cast from solutions of 9.7 and 75.7 kg/mole PS onto oxidized Si wafers, leaving films that were studied in both as-cast (samples A1 and B1) and vacuum-annealed (A2 and B2) states. Ultrathin films were spin-cast from solutions of 32 kg/mole PS onto Si_3N_4-coated Si wafers with thicknesses of $t \sqsupset 100$ *nm* (C) and 20 *nm* (D). Samples C and D spanned semitransparent membrane windows to facilitate transmission measurements, although the reflectivity and scattering data presented here were collected from regions where the films were supported by the Si substrate.   All material had polydispersity index $M_W/M_N \cong 1.05 - 1.06$.

B. Resonant scattering measurements at the carbon *K*-edge

Scattering and reflectivity measurements utilized ALS beamline 11.0.1 equipped with an elliptically polarizing undulator providing *s*- and *p*-polarized 1st harmonic radiation incident upon samples centered on a 2-axis goniometer [33]. To maximize sensitivity to anisotropic bonding we focus on energy scans at fixed angles rather than *vice versa*. An upstream, 4-bounce, Ni-coated mirror system rejects higher harmonic radiation to facilitate accurate spectroscopy in direct beam, specular reflectivity $R_{s/p}(h\nu)$, and diffuse scattering intensity $I_{s/p}(h\nu)$ measurements. A silicon diode measured the direct beam and low-angle $R_{s/p}(h\nu)$, and the direct beam spectra were used to normalize both $R_{s/p}(h\nu)$ and high-angle $I_{s/p}(h\nu)$ intensities. The $I_{s/p}$ spectra were measured with $\theta_i = 30°$ using a silicon CCD subtending 0.062 sr at $2\theta = 100°$, yielding a scattering vector **q** with magnitude $q = 2.2$ +/- 0.07 *nm*⁻¹ at 285 eV and oriented 20° off the surface normal. This *q* is well below the "polymerization" and "amorphous" peaks at 7 and 15 *nm*⁻¹ measured with hard x-rays [23, 27-29], consistent with our observation of weak, flat intensity across the CCD, whose integrated signal is thus reported.

Linear polarizers resolve polarized from depolarized (rotated) scattering components in the visible and hard x-ray spectral ranges. While specular linear polarizers exist in the soft x-ray range [16, 34, 35], they are inefficient. Because of the weak intensities and relaxed angular resolution in the diffuse scattering measurement, we did not employ a separate linear polarizer. Instead, we note that at $2\theta = 100°$ the samples themselves act as linear polarizers, strongly suppressing elastic polarized $p \rightarrow p$ scattering compared to $s \rightarrow s$ scattering.

The weak diffuse intensity signal indicates that we must distinguish between elastic scattering and possible inelastic fluorescence intensity. While the fluorescence yield of 0.0025

resulting from carbon K-edge absorption is small [36], we expect and find a contribution from fluorescence. As described below, we eliminate unpolarized fluorescence by considering $I_p - I_s$.

Comparing spectra measured with incident s- and p-polarization across the carbon edge requires care, as ubiquitous spectral signature of carbonaceous contamination on beamline optics is itself anisotropic, signaling that contamination layer bonding has, on spatial average, preferred orientation. The optical effects of such contamination are identical to those we are interested in measuring from the aPS films in specular reflectivity. We assume the contamination is described by a spatially averaged, resonant, uniaxial anisotropy with axis normal to the optical surfaces and uniform in-plane properties. In this case, incident s- and p-polarization will reflect from contaminated mirrors as the pure linear components (without polarization rotation due to resonant birefringence), thus preserving s- and p- character. Any short-range heterogeneity in anisotropy or density will scatter weakly out of the forward-scattered and specularly reflected beams, as in the diffuse scattering of interest from the aPS samples.

The beams incident on the samples are thus expected to have well-defined s- and p-character, albeit with spectral differences arising from the anisotropic contamination on the optics. In separate measurements of linearly polarized undulator radiation at ALS beamline 8.0.1 using a linear polarizer [35], we found no change in the degree or azimuth of linear polarization of the incident beam across the carbon edge, confirming that carbon contamination on optics does not alter the polarization state of incident linear s- or p- polarization.

The distinct incident s- and p-polarized spectra must be carefully monitored, as beam motion across non-uniform contamination, or changes in contamination, can cause them to vary over time. Our protocol involved frequent measurement of s- and p- direct beam spectra in series with spectra from some subset of the 6 samples in four different sessions spanning an 8-

month period. In some sessions the direct beam and/or scattered spectra showed evidence of temporal instability, presumably resulting from beam position instability. In other sessions, repeated measurements indicated relatively good stability. We systematically illuminated fresh areas of samples to minimize radiation damage. In this way we came to understand which spectral features are and are not reproducible. The $R_{s/p}(h\nu)$ and $I_{s/p}(h\nu)$ datasets below were collected in relatively stable, single measurement sessions and contain features that are robust and representative of polarization differences. This is not to say that measurement artifacts are absent in the data, but that they are small compared to the spectral features of interest.

III. RESULTS AND DISCUSSION

A. Resonant optical anisotropy from specular reflectivity

Visible optical techniques, including guided-wave measurements of spatially averaged optical anisotropy in micron thick films [19-22] and sum frequency generation (SFG) of surface anisotropy [37, 38], have revealed a tendency for phenyl rings in aPS to orient with ring axes preferentially in the plane of the films. Electron yield XAS studies [12, 13] are consistent with these visible techniques, that together benchmark our determination of laterally averaged and penetration depth weighted resonant anisotropy in aPS using low-angle specular reflectivity $R_{s/p}(h\nu)$. We likewise find preferential in-plane orientation of phenyl ring axes. Additionally, we identify an unanticipated anisotropy contribution from the polyethylene-like chain backbone.

Figure 2 shows absolute $R_{s/p}$ measured at $\theta_i = 5°$ for two thick, drop-cast films (A1 and B2) and the two ultrathin, spin-cast films (C and D). Data in panels 2a – 2d are re-plotted on an expanded scale in panels 2e – 2h, where subtle differences between R_p and R_s are more evident. The thick and ultrathin films exhibit very different behavior. Spectra from the thick samples are

8

similar to absorption spectra because measurements were made above the critical angle for total reflection and the samples appear infinitely thick at this θ_i. In contrast, spectra from ultrathin films appear more like transmission spectra with intensity dips at strong absorption features; this is because the underlying substrate partially reflects radiation transmitted by the overlying film. The ultrathin film spectra also exhibit thickness fringes that include resonant refractive effects.

Weak polarization differences for each sample in Figure 2 are pronounced at the strong phenyl ring π^* resonance near 285 eV marked by the vertical dashed line, although differences persist at other energies as well. The reflectivity anisotropy $\Delta R = R_p - R_s$ for samples A1 and B2 are plotted in Figure 3 and exhibit resonant character. $R_{s/p}$ values for B2 are roughly half those for A1, due to larger roughness, and ΔR is 3 times smaller for B2 than for A1. Both increased roughness and reduced anisotropy could result from the annealing of B2 [39]. The dominant features in ΔR below the ionization potential at 289.7 eV are coincident for both samples, and both spectra exhibit a broad negative region centered near 294 eV. For B2, ΔR returns to zero at roughly 304 eV, while for A1 the difference becomes positive at 301 eV before returning to zero at 320 eV (out of plot range). While the absolute size of $\Delta R/(R_p + R_s)$ is small, ~ 10 % at the $\pi 1^*$ line and much less at higher $h\nu$, the coincidence of these ΔR features for the thick samples indicates that they are not measurement artifacts. For the ultrathin films, the ΔR spectra (not shown) are different from each other because of differences in thin film interference effects. Anisotropic refractive effects in $R_{s/p}$ are evident near the π^* peak of samples C and D (Figs. 2g & 2h), and can explain why ΔR does not tend quickly to zero above (C) and below (D) this energy. The spectral trends of the thick samples are explored further below.

To obtain the resonant optical properties, and their anisotropy, we model $R_{s/p}$ as in spectroscopic ellipsometry assuming uniaxial anisotropy normal to the sample surfaces. This analysis differs from those used in previous studies of anisotropic carbon edge reflectivity [16-18] in that it obtains absolute optical properties directly from measured reflectivity spectra. We use a maximum entropy refinement algorithm that ensures Kramers-Kronig consistency to obtain the complex resonant monomer scattering factors $\langle f(hv) \rangle_{s/p} = \langle f_1 \rangle_{s/p} + i \langle f_2 \rangle_{s/p}$ that best fit the data [40]. Brackets indicate values spatially averaged over the x-ray coherence volume and the larger illuminated volume of the sample. The model assumes homogeneous anisotropy and infinitely thick samples. Resulting $\langle f \rangle_{s/p}$ are thus effective values consistent with these assumptions. For $\theta_i = 5°$, $\langle f \rangle_p$ is a good representation of the out-of-plane properties; at large angles this approximation may not hold [17, 41]. The spectral refinement algorithm benefits from reasonably accurate starting values for resonant optical properties, and input spectra were obtained from transmission absorption measurements of similar aPS films. The refinements for the two thick samples result in essentially perfect fits to the measured $R_{s/p}$ spectra in Figure 2a and 2b, and so are not reproduced here.

Spectral refinement results for sample A1 $\langle f_2 \rangle_{s/p}$ are in Figure 4a, normalized to a C_8H_8 monomer basis using a density of 1.04 g/cc. The resonant features are familiar from C $1s$ absorption into specific anti-bonding π^*, σ^*, and continuum states [10, 12, 13, 42]. The $\langle f_2 \rangle_{s/p}$ display essentially the same anisotropy as the $R_{s/p}$. Resonant optical anisotropy, specifically linear dichroism, $\Delta \langle f_2 \rangle = \langle f_2 \rangle_p - \langle f_2 \rangle_s$, is plotted in Fig. 4b and compared with results from previous studies below.

Reflectivity measurements clearly sense anisotropy, and differences in anisotropy between samples, so that some ambiguity must exist in uniquely describing absolute resonant

10

optical properties of polymers, even those obtained from spatially averaging techniques. These

will, in general, depend on the specific anisotropy in a given sample and the orientation of ϵ_o

relative to that anisotropy. Short of resolving optical properties along unique axes as done here,

the most meaningful description is the isotropic average given by $f_{2,iso} = (2\langle f_2 \rangle_s + \langle f_2 \rangle_p)/3$.

Values so obtained are in good agreement for samples A1 and B2.

The isotropic spectrum for A1 is plotted in Figure 5a, where its resonant features are

modeled using 3 symmetric Gaussians, 2 asymmetric Gaussians [9, 43], and an error function

step at the ionization potential (IP) representing non-resonant, continuum absorption. Table 2

lists the positions and origin of these features, and Fig. 1 provides the local monomer reference

frame. These lines represent the phenyl ring $\pi1^*$ and $\pi2^*$ resonances oriented along the ring

axes, as well as the C-H, $\sigma1^*$ and $\sigma2^*$ resonances having contributions from both the rings and

the backbone. The same IP is assumed for all C species. The use of just 3 resonance lines to

represent the mixed C-H and C-C σ^* contributions from both ring and chain bonding is an

assumption that we revisit below. Figure 5b contains the dispersive $f_{1,iso}$ terms of this model for

the complex, isotropic monomer form factor $f_{iso} = f_{1,iso} + if_{2,iso}$. While in the hard x-ray range

$f_2 \ll f_1$, at soft x-ray resonances they are comparable and both contribute to measured

scattering.

The skin or penetration depth for soft x-rays is a strong function of $h\nu$ across the edge

[44]. Thus, while infinitely thick samples were assumed to model $R(h\nu)$ from the thick samples,

the actual probing depth is much less than the film thickness at and above the $\pi1^*$ line.

The dominant anisotropy observed here is the strong negative $\pi1^*$ peak that implies some

degree of preferred orientation of ring axes in the plane of the sample. This is consistent with the

negative optical anisotropy found by Prest & Luca at $\lambda = 633$ *nm* and understood by them and

others to result from preferential alignment of chain backbones in the film plane together with steric effects constraining phenyl rings to orient with axes within +/- 25° of the local backbone direction [19-22]. Negative anisotropy at the $\pi 1^*$ peak nearly identical to that for A1 is also found in measurements of XAS anisotropy using surface sensitive partial electron yield (PEY) techniques that were likewise interpreted to result from preferential orientation of phenyl ring axes in the surface plane [12, 13]. Annealing was found to significantly reduce this XAS anisotropy [39]. Tuning the PEY approach for extreme surface sensitivity, Lenhart, *et al*., conclude that the chains at the surface exhibit additional asymmetry whereby the rings also orient proximal to the surface with their attached backbone segments away from the surface [13]. Their finding is consistent with molecular dynamics simulations [45], and with earlier results from SFG spectroscopy [37, 38]. All of these previous studies attribute the observed anisotropy entirely to the phenyl rings because of their highly anisotropic bonding.

The broad agreement that phenyl rings exhibit preferential in-plane axial alignment in aPS films validates the reflectivity-based approach used here, at least for the observed $\pi 1^*$ anisotropy.   It is reasonable to expect that resonant x-ray sensitivity to anisotropy should extend to the $\pi 2^*$ line and also to the C-H and C-C σ^* features having mixed contributions from the rings and backbone, where weaker anisotropy is expected.

Continuing to consider just the phenyl rings, we expect that the $\pi 2^*$ peak at 288.8 eV will exhibit negative anisotropy like the dominant $\pi 1^*$ peak, and find a weak negative anisotropy in ΔR and $\Delta \langle f_2 \rangle$ in Figs. 3 and 4b, respectively. Likewise, since 5 of the 8 C-H monomer bonds are in the ring plane, we expect and observe a small positive anisotropy at 287 eV. Indeed, if all of the observed anisotropy in $\Delta \langle f_2 \rangle$ were due to the phenyl rings as suggested [13, 19, 20, 37], since 7 of the 9 monomer C-C σ^* contributions are associated with the planar rings, we would expect

12

an abrupt transition from negative to positive anisotropy as the IP is crossed and the σ1* and σ2* resonances dominate. Instead, $\Delta\langle f_2 \rangle$ remains negative throughout the σ1* region and does not become positive until 297 eV, as the σ2* region is approached.

This negative $\Delta\langle f_2 \rangle$ in the σ1* region cannot result from the phenyl rings and so must result from C-C bonding in the backbone. To explore this possibility we assume that XAS from oriented polyethylene (PE) and benzene provide useful approximations for anisotropic XAS from the backbone and phenyl rings, respectively. XAS from oriented (stretched) PE reveals a very pronounced imbalance of spectral weight in the σ1* over the σ2* region when ϵ_o is oriented along the chain axes [46, 47]. It is also evident that the σ* contributions in PE are not simply distributed in the two σ1* and σ2* lines of the above model; rather, the σ1* region of our model is split into several features in PE XAS [42, 48]. XAS of oriented benzene molecules, on the other hand, shows roughly equal spectral weight in σ1* and σ2* peaks when ϵ_o is in the ring plane [49]. Negative $\Delta\langle f_2 \rangle$ in the σ1* region of aPS is consistent with a strong contribution from backbone segments having preferential orientation in the film plane, as early models predicted [19-22]. Analysis of the reflectivity anisotropy thus identifies a direct backbone σ* contribution to anisotropy in addition to the established and sharper phenyl ring π1* contribution.

While we are not aware of previous claims of direct resonant sensitivity to aPS backbone orientation, we note that weak, resonant anisotropy features in the σ1* region essentially identical to those observed here (Fig. 4) were also observed by Lenhart, *et al*. [13], (see their Figures 4 and S2b) and in an earlier study by Fischer, *et al.* [12], (see their Figure 2) using the same PEY approach. Lenhart, *et al*., conclude that these weak features are within measurement error and so do not consider them as significant. We disagree. While our negative $\Delta\langle f_2 \rangle$ anisotropy (and their XAS anisotropy) in the σ1* region is weak at a given energy, it extends

over an appreciable range yielding an area that is a considerable fraction of that of the negative

π1* peak, and of the positive σ2* peak whose sign is consistent with phenyl ring origin. This

negative σ1* anisotropy is a robust feature in ΔR measured from thick aPS samples.

Furthermore, identical features are obtained via different experimental approaches (reflectivity

and PEY), using different sources of linearly polarized synchrotron radiation (undulator and

bending magnet) and on different aPS samples. These considerations support our conclusion that

the negative anisotropy in the σ1* region results from preferential in-plane orientation of chain

backbone segments. Further evidence for a backbone anisotropy contribution comes from the

depolarized scattering measurements presented below.

B. Depolarized scattering from short-range orientation fluctuations

Exploration of resonant depolarized scattering at high momentum transfer due to the

short-range anisotropy fluctuations in otherwise homogeneous aPS was the initial motivation for

this study. This added resonant sensitivity to anisotropy represents a qualitatively different

scattering mechanism than those active in non-resonant x-ray, neutron, and electron scattering.

Formalisms incorporating anisotropic scattering centers from the visible and hard x-ray spectral

ranges are relevant and adapted here to describe polarized and depolarized contributions in

diffuse scattering measurements.

We consider that each monomer is described by an anisotropic scattering tensor that is

coarse-grained at the phenyl ring and attached backbone segment level. While clearly an

oversimplification, assume each monomer is identical with ring axis strictly parallel to the

backbone axis (Fig. 1), and with uniaxial scattering tensor $\mathbf{F} = \begin{pmatrix} f_\perp & 0 & 0 \\ 0 & f_\perp & 0 \\ 0 & 0 & f_\parallel \end{pmatrix}$ when its axis is

oriented along z. The far-field scattered intensity from a disordered assembly of anisotropic

monomers is then $I_{s/p}(h\nu) \propto \sum_i \sum_j a_i a_j^* e^{i\mathbf{q}\cdot\mathbf{r}_{ij}}$ integrated over the illuminated sample volume

with appropriate absorption corrections applied. Subscripts in $I_{s/p}$ refer to the incident

polarization $\boldsymbol{\epsilon}_{o,s/p}$, and $\mathbf{r}_{ij} = \mathbf{r}_i - \mathbf{r}_j$. Each amplitude has the form $a_i = \boldsymbol{\epsilon}_f \cdot (\mathbf{F}_i(\mathbf{r}_i, h\nu) \cdot \boldsymbol{\epsilon}_o)$,

with $\mathbf{F}_i$ the monomer tensor at $\mathbf{r}_i$ to which a rotation transform, generally yielding off-diagonal

elements, is implicit, and $\boldsymbol{\epsilon}_f$ is the scattered polarization. $\boldsymbol{\epsilon}_o$ excites dipoles according to its

orientation relative to $\mathbf{F}_i$, whose diagonal and off-diagonal elements yield polarized ($s \rightarrow s$ and p

$\rightarrow p$) and depolarized ($s \rightarrow p$ and $p \rightarrow s$) amplitude contributions, respectively. Intensity

contributions arise only from amplitudes with the same $\boldsymbol{\epsilon}_{f,s/p}$.

　　While the q-dependence of $I_{s/p}$ is usually of interest in x-ray scattering from polymers

[27-29], the same spatial arrangement of scattering centers contributes to its $h\nu$ dependence at

fixed q, which thus is sensitive to the ensemble-average, 2-point density and orientation

distribution of PS monomers. The polarized and depolarized elastic scattering contributions to

$I_{s/p}$ are related to spatial fluctuations in density and anisotropic orientation, respectively [1, 2].

To resolve these contributions without the benefit of a linear polarizer in the scattered beam, we

use the samples as polarizers to suppress polarized $p \rightarrow p$ scattering by $(\cos 2\theta)^2 = 0.03$

compared to $s \rightarrow s$ scattering. By symmetry, any θ dependence of depolarized scattering not

resulting from specific structural correlations is the same for $s \rightarrow p$ and $p \rightarrow s$ scattering.

　　Measured diffuse scattering $I_{s/p}^m(h\nu)$ from samples A2, B2, C, and D are plotted in

Figure 6 and display characteristic features, including $\boldsymbol{\epsilon}_o$ polarization anisotropy. The

superscript emphasizes that measured data may contain more than the elastic contributions in the

$I_{s/p}$ expression above. The only normalization of the $I_{s/p}^m$ is by the corresponding direct beam

spectra so that the relative intensities for different samples are meaningful. Spectra in Figs. 6a

and 6b from thick samples A2 and B2, respectively, are nearly identical. Those in Figs. 6c and 6d from ultrathin film samples C and D are more similar to each other than to those from the thick samples. While features familiar from resonant XAS are evident for all samples, so are pronounced differences. Resonant features at the π1* and σ1* positions dominate $I_{s/p}^m$ in the thick films, while the other resonant lines are increasingly evident as t decreases in the ultrathin films.

The diffuse difference spectra, $\Delta I^m = I_p^m - I_s^m$, are collected in Figure 7 and exhibit characteristic intensity reversal between sharp, positive and broad, negative peaks in the phenyl π1* and backbone σ1* regions, respectively. The ΔI^m show much less difference between the thick and ultrathin samples than do the individual $I_{s/p}^m$ spectra. The π1* peaks in ΔI^m occur at the peaks in $I_{s/p}^m$, and both are shifted somewhat below the π1* peak at 285.0 eV due to strong absorption and refractive contributions to scattering. Some drift evident as small vertical offsets in the different ΔI^m, and non-zero limiting trends, presumably results from artifacts discussed above; artifacts due to temporal instabilities affect the slower diffuse measurements more than the faster specular measurements.

Before considering possible structural origins within aPS for these resonant features, we must determine what scattering mechanisms contribute to I_s^m, I_p^m and their difference. We consider inelastic fluorescence as well as polarized and depolarized elastic scattering from internal structure and from surface roughness, and utilize their known symmetry relative to ϵ_o.

An unpolarized fluorescence contribution is expected, especially in I_p^m, since polarized p → p elastic scattering is strongly suppressed. Any fluorescence is expected to exhibit thickness dependent intensity and saturation effects as t varies across the skin depth at $\theta_i = 30°$ used in these diffuse measurements. From the $f_{2,iso}$ determined above it is straightforward to calculate

the approximate fluorescence contribution [44]. The results are plotted as dashed lines in the different panels of Fig. 6. Extremely strong saturation effects are evident, pervading the fluorescence spectra for the thick samples A2 and B2 and decreasing with t for C and D. The relative shapes and intensities of these calculated fluorescence contributions evidently do account for a significant portion of measured $I_{s/p}^m(hv)$, specifically, the growth of the featureless IP step relative to the resonant absorption lines as t increases. We conclude that, to a good approximation, the difference ΔI^m removes unpolarized fluorescence, leaving a sizable residue of elastic scattering.

We next consider polarized and depolarized elastic scattering contributions in $I_{s/p}$, described by the above expression. Small-angle, polarized elastic scattering from aPS using hard x-rays to study density fluctuations is well established in thick and ultrathin samples [23-26], and with $q = 2.2 \ nm^{-1}$ the soft x-ray data here are within the typical SAXS range. The large suppression of $p \to p$ scattering in the soft x-ray measurement, combined with the observations that $I_s^m \cong I_p^m$ and that ΔI^m varies systematically about 0 for all samples (Fig. 6) reveals that $s \to$ s scattering, likewise, cannot contribute appreciably. Polarized, diffuse elastic scattering from surface roughness is also expected from density contrast between the vacuum and the average sample density [50], and has been measured in hard x-ray studies of surface roughness from aPS films at in-plane q values roughly 100 times smaller than in our measurement [30-32]. The same symmetry argument applies to a possible contribution from polarized surface scattering in the soft x-ray measurement, with the same result. We thus conclude that any polarized elastic scattering from internal film structure or surface roughness contributing to $I_{s/p}^m$ is weak compared to fluorescence and depolarized elastic scattering in these measurements. Furthermore, the

17

residual ΔI^m must result from depolarized elastic scattering from orientation fluctuations internal to the samples.

The ΔI^m spectra in Figure 6 thus represent differences in depolarized elastic scattering with incident polarization. The dependence on $\boldsymbol{\epsilon}_o$ implies anisotropy of the short-range orientation fluctuation texture in the films; if the orientation fluctuations and average orientation of monomers were isotropic [1, 51] their depolarized components would cancel in ΔI^m and depolarized scattering could only be observed in $I^m_{s/p}$ along with the unpolarized fluorescence. Understanding that ΔI^m measures the anisotropy of the depolarized scattering, we can now consider its origin in terms of the anisotropy of short-range orientation fluctuations.

All of the ΔI^m have very similar shape characterized by prominent positive and negative peaks at the phenyl $\pi 1^*$ peak and the backbone $\sigma 1^*$ region, respectively. There are no distinct features in the $\sigma 2^*$ region. The intensity of these features is weakest for the thickest samples, suggesting that orientation fluctuations are more isotropic in thicker samples. However this is not obvious for different reasons. One is that even with $\theta_i = 30°$, the penetration into the sample is limited to well below the thickness of samples A2 and B2 [44]. Another is that t-dependent absorption corrections, similar to but distinct those used to calculate fluorescence [44] also apply to the elastic scattering. Aside from changes in intensity, the shape of ΔI^m is clearly characteristic of aPS. To understand what mechanisms yield the depolarized contributions to ΔI^m and $I^m_{s/p}$, and hence what information they contain, we revisit certain experimental details and previous studies of aPS.

Depolarized scattering results when the orientation of anisotropic scattering centers changes over a distance of order $2\pi/q \cong 2.9 \ nm$, and its strength scales with the ensemble average of the amount of this orientation decorrelation. For comparison, characteristic length

scales in aPS include the closest average phenyl-phenyl spacing of ⬚ 0.6 *nm*, the distance of

closest chain backbone approach set by excluded volume effects of ⬚ 1 *nm*, and the chain

persistence length or half the Kuhn length of ⬚ 1 *nm*. The extrema in $\Delta I^m(h\nu)$ at the phenyl $\pi 1^*$

and backbone $\sigma 1^*$ peaks indicate that orientation fluctuations of both entities yield scattering.

The separation of these peaks in f_{iso} (Fig. 5) suggests that phenyl-phenyl and backbone-

backbone contributions may be stronger than phenyl-backbone contributions to depolarized

intensity, based simply on spectral considerations. The depolarized scattering contains

contributions of these three partial structure factors, representing distinct types of orientation

fluctuations at several times the closest chain backbone approach and chain persistence length.

With **q** directed 20° from the surface normal, orientation decorrelation roughly normal to

the surface is probed by $I_{s/p}$. The tendency for in-plane chain alignment implies that

intermolecular correlations are sampled somewhat more than intramolecular correlations in this

direction. In addition to relative orientation differences along **q**, the average preferential

orientation of anisotropic entities relative to **q** influences ΔI^m spectral features through the

excitation of the $\mathbf{F}_i$ by $\boldsymbol{\epsilon}_o$. Thus variation in the in-plane preferential chain alignment direction is

sensed more strongly by *s*- than by *p*-polarization along **q** and can explain the negative

anisotropy at the backbone $\sigma 1^*$ peak. Positive anisotropy at the phenyl peak indicates stronger

phenyl-phenyl orientation decorrelation sensed by *p*- than by *s*-polarization. Evidently the

additional orientational degrees of freedom of the rings about the backbone cause the depolarized

scattering from the rings to exhibit distinctly different character than that from the backbone.

Further insight relating measured depolarized scattering anisotropy to statistics of

orientation decorrelation and chain conformation will be aided by comparison with structural

models for aPS. While beyond the scope of this work, we can anticipate some aspects of such

studies. Structural models from molecular dynamics and Monte Carlo simulations are readily resolved into intra- and intermolecular partial distribution functions and partial structure factors for phenyl-phenyl, backbone-backbone, and phenyl-backbone correlations for comparison with hard x-ray and neutron scattering results [29, 52, 53]. Extending these to include tensor scattering entities and evaluation of resonant polarized and depolarized scattering is possible at different levels of sophistication. At one end of the scale, the various contributions to f_{iso} can be parsed into hypothetical anisotropic monomer tensor components of $\mathbf{F}_i$, positioned and oriented according to a structural model for aPS, and tested against measured scattering. At the other end, *ab initio* DFT calculations of resonant scattering factors [18, 54-58] of carbon atoms in quantum MD models [59] could be coarse-grained at the functional group, monomer, or larger level and used to calculate scattering. This latter approach can directly explore the extent to which monomer scattering properties $\mathbf{F}_i$ are identical and independent of non-bonding chain conformation effects, and to more directly explore the backbone and phenyl contributions to both spatially-averaged reflectivity and spatially-resolved scattering.

In considering the q dependence of scattering from such models, while the positions $\mathbf{r}_i$ of the tensor entities representing phenyl rings and backbone segments are identical to those used to model charge or nuclear scattering density, the length scales of orientation decorrelation are generally larger than the correlation length of the density fluctuations. Furthermore, the decorrelation lengths of backbone-backbone and phenyl-phenyl depolarized scattering will generally not be the same. One example of longer length scales probed by depolarized scattering in aPS involves stereochemical effects. The distribution of phenyl groups in dextro and levo diads imparts local helicity of opposite handedness that can extend into longer sequences, and each sequence will induce helicity dependent resonant optical rotation of incident linear

20

polarization. Depolarized resonant scattering from localized helical motifs is thus expected in aPS even of racemic constitution, and may complement NMR sensitivity to such structure [60]. Such scattering may be strongest in phenyl-backbone cross terms, as both constituents define the local chirality.

The negligible contribution of polarized compared to depolarized elastic intensity at $q = 2.2\ nm^{-1}$ is noteworthy, and confirms that off-diagonal scattering prevails at longer length scales than the shorter range density fluctuations whose scattering exhibits peaks at higher q, at least in aPS. Thus, in order to compare measured depolarized scattering with numerical structural models, such models will need to treat larger volumes than for comparison with isotropic charge scattering alone.

C. Discussion

Both sets of results above demonstrate direct sensitivity to resonant molecular anisotropy in organic systems via scattering at the carbon K-edge that will extend to the N and O K-edges. Analogous to sensitivity to anisotropy in the visible spectral region, soft x-ray measurements can sense structure in the 1 - 100 nm range, and the resonances provide added element and chemical-bond sensitivity. Compared to hard x-ray, neutron, and electron scattering, resonant effects bring fundamentally new sensitivity to the symmetry of the antibonding molecular orbital structure whose potential to provide new insight into orientational texture in soft condensed matter is not well recognized by the growing community using resonant soft x-ray scattering to enhance contrast from compositional differences in polymers. Discussion below highlights different aspects of this sensitivity, referring to the results presented here and extending to consider directions in soft condensed matter that may benefit from it.

Spectroscopic evidence for the anisotropic chain backbone contribution in the σ1* region was not anticipated at the outset of this study; the stronger, sharper resonances of the phenyl rings were expected to dominate. We came to understand its role by its presence in the anisotropy spectra of both reflectivity and diffuse scattering data. Backbone anisotropy in the σ1* region is necessary to interpret the results of each measurement individually, and its presence in both sets of results strongly confirms its existence. This highlights the value of analyzing the polarization dependence of resonant scattering spectra, that in turn derives from the spectral separation of features from different bonding motifs at the carbon K-edge. Note that σ* spectral features, and hence sensitivity to backbone anisotropy, are not accessible in the visible spectral range. The rich information regarding molecular anisotropy from XAS is generally expected to transfer to resonant scattering.

The different spatial averaging inherent in specular reflectivity and diffuse scattering explains the different size and character of the phenyl ring and backbone anisotropies in the two measurements. The measured reflectivity asymmetry $\Delta R/(R_p + R_s)$ is much smaller than the diffuse scattering asymmetry $\Delta I^m/(I_p^m + I_s^m)$ for these aPS samples, even without accounting for unpolarized fluorescence contribution in $I_{s/p}^m$. In $\Delta\langle f_2\rangle$ obtained from reflectivity modeling, if phenyl π* anisotropy is negative, then phenyl σ* anisotropy must be positive, *i.e.*, the measured anisotropy is referenced to the average orientation of rings in the illuminated sample volume relative to ϵ_o.

The relative contributions of π* and σ* features from the same functional group enter into the depolarized scattering anisotropy ΔI^m differently than into ΔR or $\Delta\langle f_2\rangle$. Scattering from orientation decorrelation scales similarly for the π* and σ* terms from nearby functional groups of the same kind, so that in a hypothetical system in which the backbone is removed, the peaks in

$I_{s/p}(h\nu)$ for the phenyl π^* and σ^* contributions will increase or decrease together for a given polarization, and so have the same sign in ΔI^m. Thus the observed opposite signs of ΔI^m in the $\pi 1^*$ and $\sigma 1^*$ regions indicates the strength of the negative $\sigma 1^*$ contribution from the chain backbones in aPS. While ensemble averaging over short-range orientation decorrelation in diffuse scattering makes the structural origin of the depolarized scattering challenging to interpret without reference to structural models, the signs of the positive and negative peaks in ΔI^m relate to the strength of orientation decorrelation along $\mathbf{q}$ of the phenyl π^* and σ^* and the backbone σ^* sensed by $\boldsymbol{\epsilon}_{o,p}$ (mostly out-of-plane) and by $\boldsymbol{\epsilon}_{o,s}$ (mostly in-plane).

Most carbon K-edge scattering studies of polymers to date have implicitly assumed homogeneous, isotropic resonant optical properties for a given phase, and some have successfully modeled $h\nu$ or q dependence of reflectivity or diffuse scattering [15, 61-65]. Several studies have noted inconsistencies between resonant optical properties measured using one technique or sample and applied to model data from another technique or sample [14, 17, 66, 67]. The present work indicates that different sensitivity to anisotropy in different measurements, or physical differences in anisotropy in different samples, or both, are possible if not likely explanations for such inconsistencies.

The assumption of homogeneous and isotropic spatially averaged resonant properties is generally open to question in highly disordered polymers, even in systems that approximate random coil behavior. The aPS anisotropy from modeling $R_{s/p}$ found here is an effective value consistent with the assumption of homogeneity. It is accepted that confinement effects in disordered homopolymers can induce ordering near interfaces [12, 45, 68-70], and that such alignment, and hence resulting resonant optical anisotropy, will generally decrease away from the interfaces. From the analysis of reflectivity data at one angle presented here, it is impossible

23

to draw conclusions about possible inhomogeneous optical anisotropy in depth. Analysis of data measured at several incidence angles does facilitate such depth-dependent modeling of changing resonant optical properties [17, 40, 71]. As polymer chains and interactions deviate further from random coil behavior, such as in conjugated polymers, we can expect increasing optical anisotropy effects in homopolymer films.

In polymers with compositional heterogeneity, such as phase-separated systems, the effects of resonant anisotropy will manifest differently depending on the anisotropy of the different phases. In determinations of the morphology of phase separated block copolymer structure via resonant scattering, *e.g*., if both phases are nominally amorphous the assumption of optical isotropy for the phases may be well-justified, especially at low q where random short-range anisotropy may average to near zero. Potentially interesting, hypothetical exceptions include cases in which the reduced dimensionality of the phases may itself induce anisotropy of the constituent chains relative to the interfaces. In cases of a crystalline phase in a disordered matrix, such as P3HT/PCBM and similar systems of interest for bulk heterojunction devices, each crystallite will scatter as a tensor and thus exhibit depolarized scattering along with possible polarized scattering from associated density fluctuations.

Sensitivity to resonant anisotropy through depolarized scattering should find utility in studies relating short- and intermediate-range molecular conformation to properties of practical and fundamental interest, provided care is exercised in addressing challenges imposed by weak scattering, inefficiency of linear polarizers, and the possible presence of resonant fluorescence and polarized elastic contributions. Correlating charge and mass transport with spatially averaged anisotropy and short-range anisotropy texture in organic electronics and polymer electrolytes, respectively, are areas of potentially fruitful application. In studies of phase

transitions in polymers, liquid crystals, and ionic and molecular liquids, depolarized scattering will allow changes in the short-range orientational texture of constituents to be quantified with unprecedented sensitivity. For example, the melting of just the alkyl chains within a system whose other structural constituents remains ordered, may be resolvable as an increase in diffuse scattering at specific q values and energies. Relating the extent of short- and intermediate-range orientational order to the crystallization or glass-forming behavior of molecular systems is a potential area of broad interest. Parallel development of structural models extending to anisotropic scattering properties may be an important aspect of such studies.

In this study, the polarization anisotropy ΔI^m was used to remove unpolarized and unwanted fluorescence, and the sample as a linear polarizer for sensing differences in $s \rightarrow s$ and $p \rightarrow p$ elastic scattering, leading to the conclusion that polarized scattering is weak compared to depolarized scattering and fluorescence at measured q values for aPS. Similar analysis will be useful in other cases, although the strength of these different contributions will depend strongly on the structure in the materials of interest. Samples act as linear polarizers to suppress $p \rightarrow p$ scattering at the C edge when probing short length scales in the narrow range of roughly 2.6 - 3.8 nm. Most polymers of current interest are not as homogeneous as aPS, with many having designed heterogeneity in the form of microphase separation with characteristic dimensions of 10 or more nanometers that will produce more polarized scattering. To separate polarized from depolarized scattering at longer length scales and over a significant q range, separate linear polarizers in the scattered beam will be required. As illustrated here, specific sample details and scattering geometries will interact in determining how molecular anisotropy effects will contribute along with other possible signals to measured intensities.

IV. Conclusions

This study of molecular anisotropy effects in resonant soft x-ray scattering used polystyrene as a well-characterized system to investigate previously unexplored depolarized diffuse scattering at high momentum transfers resulting from short-range orientation fluctuations of its functional groups. While motivated by analogs in the visible and hard x-ray spectral ranges, the details specific to measuring and analyzing depolarized diffuse scattering at the carbon K-edge are rather different and explored systematically here for the first time. We find that resonant depolarized elastic intensity and fluorescence are stronger than any polarized elastic component at $q \cong 2.2 \ nm^{-1}$. Removing the unpolarized fluorescence yields a characteristic anisotropy spectrum of depolarized scattering that contains a strong, anticipated component from the phenyl rings in addition to an even stronger, unanticipated contribution from the chain backbone. We also quantified the resonant optical anisotropy in spatially averaging, low-angle reflectivity measurements, where again expected and unexpected contributions of phenyl rings and chain backbone, respectively, are evident. The spatially averaged anisotropy agrees with previous visible and x-ray absorption results.

This work extends previous carbon K-edge studies of spatially averaged optical anisotropy via reflectivity [16-18] into the spatially-resolving regime using depolarized scattering from spatial orientation fluctuations of anisotropic functional groups. Direct sensitivity to orientation fluctuations is not available in hard x-ray (or neutron and electron) scattering studies of polymers because the resonant part of the charge scattering term is not significant. The wavelengths available at the C, N, and O K-edges yield sensitivity down to conformational length scales where many properties are determined. Careful analysis of the energy, polarization, and q dependence of depolarized, and polarized, resonant scatteringwill

provide new opportunities to gain insight into the relationship between short- and intermediate-range structure and properties in polymers and soft condensed matter.

Corresponding author: jbkortright@lbl.gov

REFERENCES

[1] R. S. Stein, and P. R. Wilson, Journal of Applied Physics **33**, 1914 (1962).

[2] B. J. Berne, and R. Pecora, *Dynamic Light Scattering* (John Wiley & Sons, New York, 1976).

[3] L. D. Barron, *Molecular Light Scattering and Optical Activity* (Cambridge University Press, Cambridge, 2004).

[4] T. Scharf, *Polarized Light in Liquid Crystals and Polymers* (John Wiley & Sons, Inc., Hoboken, NJ, 2007).

[5] D. H. Templeton, and L. K. Templeton, Acta Crystallographica Section A **36**, 237 (1980).

[6] D. H. Templeton, and L. K. Templeton, Acta Crystallographica Section A **38**, 62 (1982).

[7] V. E. Dmitrienko, Acta Crystallographica Section A **39**, 29 (1983).

[8] P. Mach, R. Pindak, A. M. Levelut, P. Barois, H. T. Nguyen, C. C. Huang, and L. Furenlid, Physical Review Letters **81**, 1015 (1998).

[9] J. Stohr, and D. A. Outka, Physical Review B **36**, 7891 (1987).

[10] J. Stohr, *NEXAFS Spectroscopy* (Springer-Verlag, Berlin, 1992).

[11] H. Ade, and B. Hsiao, Science **262**, 1427 (1993).

[12] D. A. Fischer, G. E. Mitchell, A. T. Yeh, and J. L. Gland, Applied Surface Science **133**, 58 (1998).

[13] J. L. Lenhart, D. A. Fischer, T. L. Chantawansri, and J. W. Andzelm, Langmuir **28**, 15713 (2012).

[14] C. Wang, T. Araki, and H. Ade, Applied Physics Letters **87**, 214109 (2005).

[15] G. E. Mitchell, B. G. Landes, J. Lyons, B. J. Kern, M. J. Devon, I. Koprinarov, E. M. Gullikson, and J. B. Kortright, Applied Physics Letters **89**, 124106 (2006).

[16] H. C. Mertins, P. M. Oppeneer, S. Valencia, W. Gudat, F. Senf, and P. R. Bressler, Physical Review B **70**, 235106 (2004).

[17] M. Mezger, B. Jerome, J. B. Kortright, M. Valvidares, E. M. Gullikson, A. Giglia, N. Mahne, and S. Nannarone, Physical Review B **83**, 155406 (2011).

[18] L. Pasquali, S. Mukherjee, F. Terzi, A. Giglia, N. Mahne, K. Koshmak, V. Esaulov, C. Toccafondi, M. Canepa, and S. Nannarone, Physical Review B **89**, 045401 (2014).

[19] W. M. Prest, and D. J. Luca, Journal of Applied Physics **50**, 6067 (1979).

[20] W. M. Prest, and D. J. Luca, Journal of Applied Physics **51**, 5170 (1980).

[21] A. E. Tonelli, Macromolecules **6**, 682 (1973).

[22] D. Y. Yoon, P. R. Sundararajan, and P. J. Flory, Macromolecules **8**, 776 (1975).

[23] G. D. Wignall, D. G. H. Ballard, and J. Schelten, European Polymer Journal **10**, 861 (1974).

[24] R. J. Roe, and J. J. Curro, Macromolecules **16**, 428 (1983).

[25] M. K. Mukhopadhyay, X. Jiao, L. B. Lurio, Z. Jiang, J. Stark, M. Sprung, S. Narayanan, A. R. Sandy, and S. K. Sinha, Physical Review Letters **101**, 115501 (2008).

[26] M. K. Mukhopadhyay, L. B. Lurio, Z. Jiang, X. Jiao, M. Sprung, C. DeCaro, and S. K. Sinha, Physical Review E **82**, 011804 (2010).

[27] G. R. Mitchell, and A. H. Windle, Polymer **25**, 906 (1984).

[28] H. R. Schubach, E. Nagy, and B. Heise, Colloid and Polymer Science **259**, 789 (1981).

[29] M. Mondello, H. J. Yang, H. Furuya, and R. J. Roe, Macromolecules **27**, 3566 (1994).

[30] J. Wang, M. Tolan, O. H. Seeck, S. K. Sinha, O. Bahr, M. H. Rafailovich, and J. Sokolov, Physical Review Letters **83**, 564 (1999).

[31] H. Kim, A. Ruhm, L. B. Lurio, J. K. Basu, J. Lal, D. Lumma, S. G. J. Mochrie, and S. K. Sinha, Physical Review Letters **90** (2003).

[32] Z. Jiang, H. Kim, X. Jiao, H. Lee, Y. J. Lee, Y. Byun, S. Song, D. Eom, C. Li, M. H. Rafailovich, L. B. Lurio, and S. K. Sinha, Physical Review Letters **98** (2007).

[33] E. Gann, A. T. Young, B. A. Collins, H. Yan, J. Nasiatka, H. A. Padmore, H. Ade, A. Hexemer, and C. Wang, Review of Scientific Instruments **83**, 045110 (2012).

[34] J. B. Kortright, and J. H. Underwood, Nuclear Instruments & Methods in Physics Research Section a-Accelerators Spectrometers Detectors and Associated Equipment **291**, 272 (1990).

[35] J. B. Kortright, M. Rice, and K. D. Franck, Review of Scientific Instruments **66**, 1567 (1995).

[36] W. Bambynek, C. D. Swift, Craseman.B, H. U. Frend, P. V. Rao, R. E. Price, H. Mark, and R. W. Fink, Reviews of Modern Physics **44**, 716 (1972).

[37] K. S. Gautam, A. D. Schwab, A. Dhinojwala, D. Zhang, S. M. Dougal, and M. S. Yeganeh, Physical Review Letters **85**, 3854 (2000).

[38] K. A. Briggman, J. C. Stephenson, W. E. Wallace, and L. J. Richter, Journal of Physical Chemistry B **105**, 2785 (2001).

[39] W. L. Wu, S. Sambasivan, C. Y. Wang, W. E. Wallace, J. Genzer, and D. A. Fischer, European Physical Journal E **12**, 127 (2003).

[40] K. H. Stone, S. M. Valvidares, and J. B. Kortright, Physical Review B **86**, 024102 (2012).

[41] D. W. Berreman, Journal of the Optical Society of America **62**, 502 (1972).

[42] O. Dhez, H. Ade, and S. G. Urquhart, Journal of Electron Spectroscopy and Related Phenomena **128**, 85 (2003).

[43] D. A. Outka, J. Stohr, J. P. Rabe, and J. D. Swalen, Journal of Chemical Physics **88**, 4076 (1988).

[44] See Supplemental Material at [...url] for details on the calculation of skin depth and approximate fluorescence intensity contributions.

[45] T. C. Clancy, J. H. Jang, A. Dhinojwala, and W. L. Mattice, Journal of Physical Chemistry B **105**, 11493 (2001).

[46] J. Stohr, D. A. Outka, K. Baberschke, D. Arvanitis, and J. A. Horsley, Physical Review B **36**, 2976 (1987).

29

[47] T. Ohta, K. Seki, T. Yokoyama, I. Morisada, and K. Edamatsu, Physica Scripta **41**, 150 (1990).

[48] Y. T. Wang, Y. Zou, T. Araki, L. N. Jan, A. L. D. Kilcoyne, J. Sokolov, H. Ade, and M. Rafailovich, Macromolecules **43**, 8153 (2010).

[49] J. A. Horsley, J. Stohr, A. P. Hitchcock, D. C. Newbury, A. L. Johnson, and F. Sette, Journal of Chemical Physics **83**, 6099 (1985).

[50] S. K. Sinha, E. B. Sirota, S. Garoff, and H. B. Stanley, Physical Review B **38**, 2297 (1988).

[51] R. S. Stein, P. F. Erhardt, S. B. Clough, and G. Adams, Journal of Applied Physics **37**, 3980 (1966).

[52] R. J. Roe, M. Mondello, H. Furuya, and H. J. Yang, Macromolecules **28**, 2807 (1995).

[53] C. Ayyagari, D. Bedrov, and G. D. Smith, Macromolecules **33**, 6194 (2000).

[54] V. Carravetta, H. Agren, L. G. M. Pettersson, and O. Vahtras, Journal of Chemical Physics **102**, 5589 (1995).

[55] S. G. Urquhart, A. P. Hitchcock, A. P. Smith, H. Ade, and E. G. Rightor, Journal of Physical Chemistry B **101**, 2267 (1997).

[56] L. G. M. Pettersson, H. Agren, B. L. Schurmann, A. Lippitz, and W. E. S. Unger, International Journal of Quantum Chemistry **63**, 749 (1997).

[57] S. G. Urquhart, A. P. Hitchcock, A. P. Smith, H. W. Ade, W. Lidy, E. G. Rightor, and G. E. Mitchell, Journal of Electron Spectroscopy and Related Phenomena **100**, 119 (1999).

[58] B. Brena, G. V. Zhuang, A. Augustsson, G. Liu, J. Nordgren, J. H. Guo, P. N. Ross, and Y. Luo, Journal of Physical Chemistry B **109**, 7907 (2005).

[59] J. S. Uejio, C. P. Schwartz, R. J. Saykally, and D. Prendergast, Chemical Physics Letters **467**, 195 (2008).

[60] P. Robyr, Z. Gan, and U. W. Suter, Macromolecules **31**, 8918 (1998).

[61] T. Araki, H. Ade, J. M. Stubbs, D. C. Sundberg, G. E. Mitchell, J. B. Kortright, and A. L. D. Kilcoyne, Applied Physics Letters **89**, 124106 (2006).

[62] J. M. Virgili, Y. F. Tao, J. B. Kortright, N. P. Balsara, and R. A. Segalman, Macromolecules **40**, 2092 (2007).

[63] D. T. Wong, C. Wang, K. M. Beers, J. B. Kortright, and N. P. Balsara, Macromolecules **45**, 9188 (2012).

[64] A. C. Stuart, J. R. Tumbleston, H. X. Zhou, W. T. Li, S. B. Liu, H. Ade, and W. You, Journal of the American Chemical Society **135**, 1806 (2013).

[65] S. Swaraj, C. Wang, H. P. Yan, B. Watts, L. N. Jan, C. R. McNeill, and H. Ade, Nano Letters **10**, 2863 (2010).

[66] C. F. Welch, R. P. Hjelm, J. T. Mang, M. E. Hawley, D. A. Wrobleski, E. B. Orler, and J. B. Kortright, Journal of Polymer Science Part B-Polymer Physics **51**, 149 (2013).

[67] H. P. Yan, C. Wang, A. R. McCarn, and H. Ade, Physical Review Letters **110**, 177401 (2013).

[68] P. G. deGennes, *Scaling Concepts in Polymer Physics* (Cornel University Press, Ithaca, New York, 1979).

[69] S. H. Anastasiadis, T. P. Russell, S. K. Satija, and C. F. Majkrzak, Physical Review Letters **62**, 1852 (1989).

[70] B. J. Factor, T. P. Russell, and M. F. Toney, Physical Review Letters **66**, 1181 (1991).

[71] S. M. Valvidares, M. Huijben, P. Yu, R. Ramesh, and J. B. Kortright, Physical Review B **82**, 235410 (2010).

Table 1. Atactic polystyrene samples cast from toluene solutions.

Sample	M_W (kg/mole)	Casting method	Post cast processing	Thickness (*nm*)	Substrate
A1	9.7	Drop cast	As-cast	1612[a]	Oxidized Si
A2	9.7	Drop cast	Vacuum @ 140 C, 8 hrs	1623[a]	Oxidized Si
B1	95.7	Drop cast	As-cast	2093[a]	Oxidized Si
B2	95.7	Drop cast	Vacuum @ 140 C, 8 hrs	2047[a]	Oxidized Si
C	32	Spin cast	Vacuum, 3 hrs	100[b]	Si$_3$N$_4$ coated Si
D	32	Spin cast	Vacuum, 3 hrs	20[b]	Si$_3$N$_4$ coated Si

[a]Measured using a visible reflectometer.

[b]Designed thickness (not directly measured).

Table 2. Positions and identification of spectral features in aPS isotropic absorption spectrum given by $f_{2,iso}$ and shown in Figure 5a. The definition of the local (monomer) phenyl ring and backbone axes are found in Figure 1.

| Feature	hν (eV)	Nominal Origin
π1*	285.0	6 C=C bonds along phenyl ring axis, no backbone contribution
C-H	287.1	5 bonds in phenyl ring plane, 3 in backbone orthogonal to axis
π2*	288.8	6 C=C bonds along phenyl ring axis, no backbone contribution
IP	289.7	Isotropic, assumed equal for all carbons
σ1*	293.1	7 bonds in phenyl ring plane, 3 predominantly along backbone
σ2*	301.9	7 bonds in phenyl ring plane, 3 predominantly along backbone
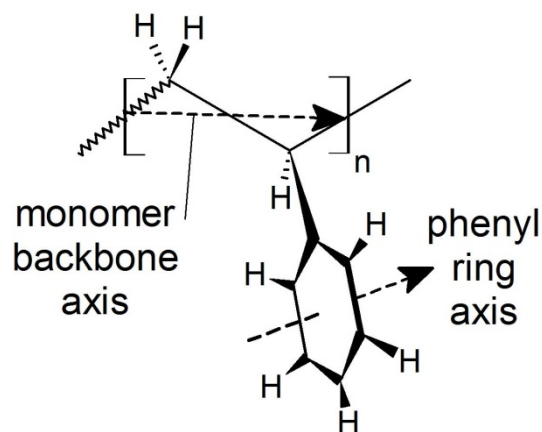
Figure 1. Polystyrene monomers, C_8H_8, consist of a relatively rigid, planar phenyl ring attached to a relatively flexible polyethylene backbone. Each phenyl ring has a unique axis along which its π system resonates, while its C-C and C-H σ bonds resonate normal to this axis in the ring plane. The monomer backbone axis vector spans the backbone segment as shown; backbone C-C and C-H σ bonds have largest projections along and orthogonal to this local direction, respectively. With the 2 C-C backbone bonds shown as solid, straight lines in the plane of the page, all other monomer bonds are generally out of the plane, and the directions of the backbone and ring axes do not coincide. In extended polymer chains, bonding and steric constraints allow considerable freedom in the orientation of the phenyl rings of different monomers. In atactic polystyrene (aPS) clockwise and counterclockwise azimuthal rotation of adjacent monomers about their connecting bond is random, leading to an amorphous structure with localized chiral regions along the chains. Coarse-graining at the monomer backbone and phenyl ring level is assumed here, and the spatial average and variation in the orientation of these distinct monomer axes is the source of the optical anisotropy and depolarized scattering effects discussed.
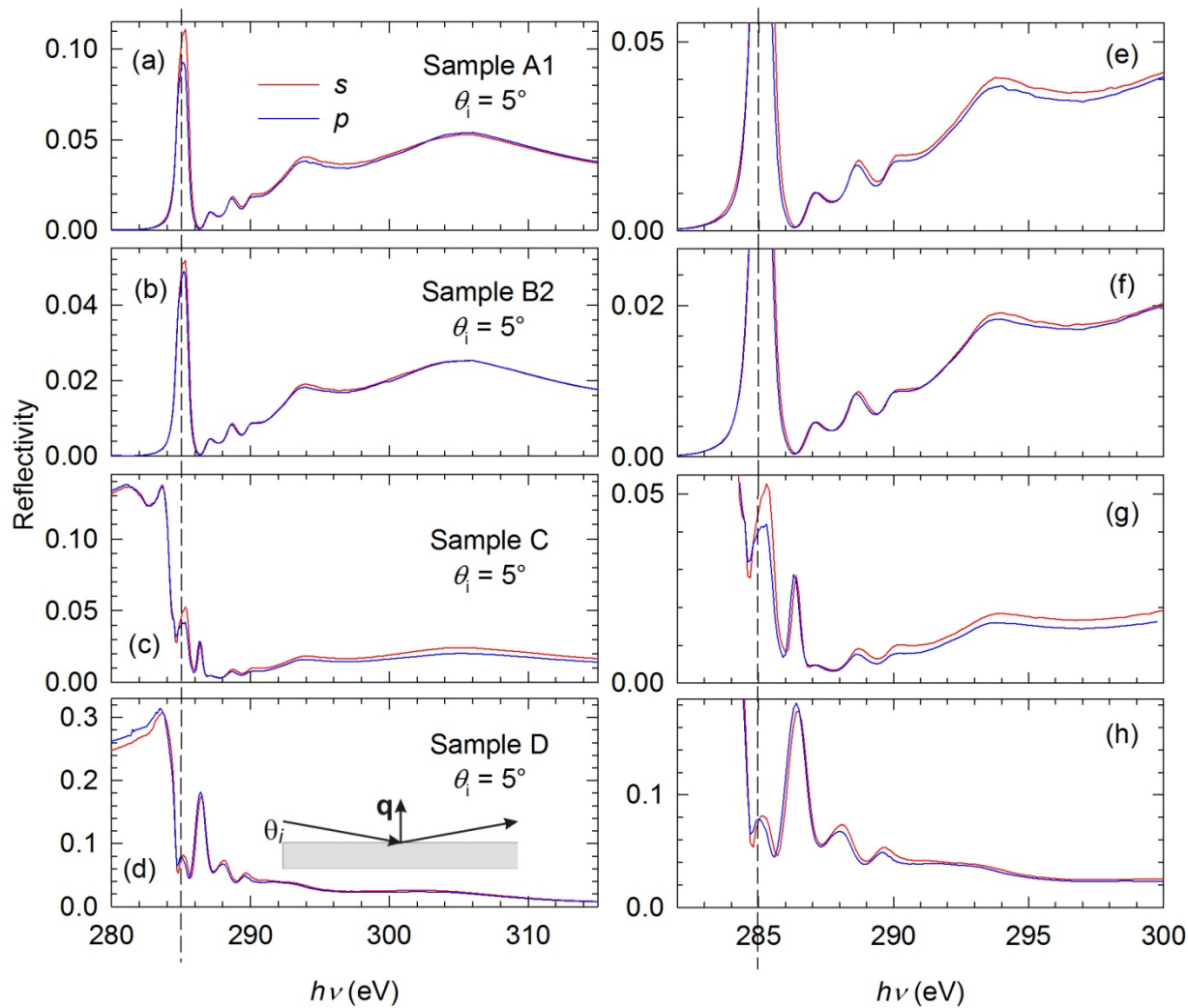
Figure 2. (Color online) (a - d) Normalized specular reflectivity spectra from four aPS samples, as noted, obtained with incident *s*- and *p*-polarized radiation at grazing incidence angle $\theta_i = 5°$; (e - h) show the same data on a magnified scale. The vertical dashed line at 285 eV marks the position of the strong $\pi 1^*$ feature from the phenyl rings.
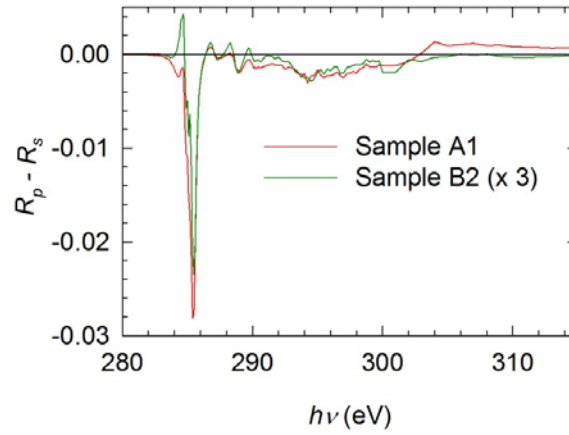
Figure 3. (Color online) Reflectance anisotropy for two thick samples A1 and B2. Data for B2 have been scaled by 3. The structure between 284 and 284.75 eV, just below the strong π^* line, occurs at deep minima especially in both the *p*-polarized incident beam spectra (due to the carbon contamination) and reflectance spectra; we disregard this narrow spectral region as possibly containing experimental artifacts.
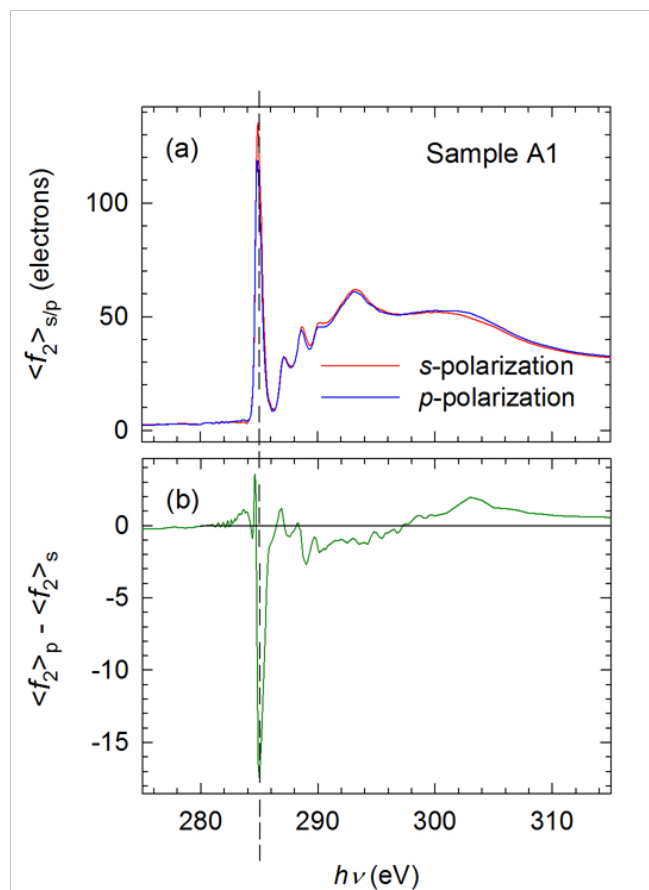
Figure 4. (Color online) (a) Spatially averaged $\langle f_2 \rangle_{s/p}$ spectra obtained from modeling the $R_{s/p}$ spectra assuming homogeneous, uniaxial anisotropy in a semi-infinite sample. (b) The resulting resonant optical anisotropy or linear dichroism. The vertical line marks the position of the strong $\pi 1^*$ line oriented along the phenyl ring axes.
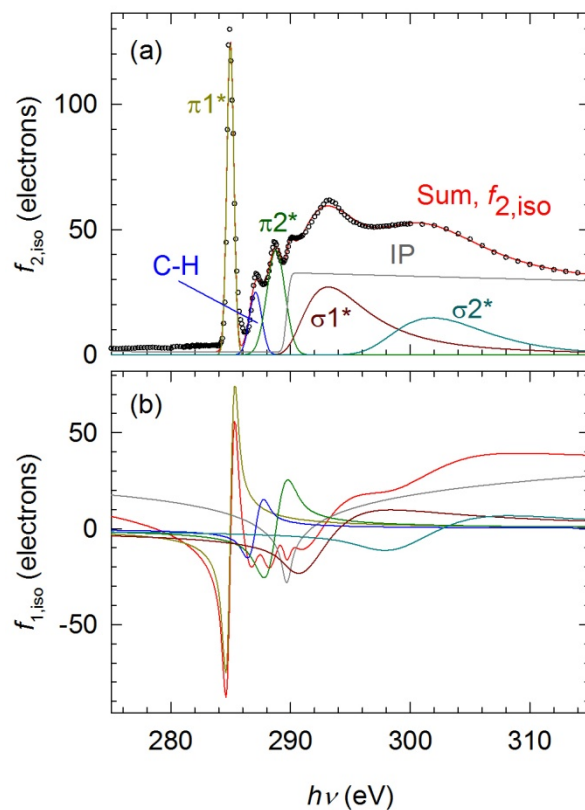
Figure 5. (Color online) The absorptive (a) and dispersive (b) parts of isotropic resonant monomer scattering factor $f_{iso} = f_{1,iso} + if_{2,iso}$ for aPS. Symbols in (a) are obtained from the weighted average of $\langle f_2 \rangle_s$ and $\langle f_2 \rangle_p$ from Fig. 4a, and lines represent a fit to these data using 3 symmetric Gaussians, 2 asymmetric Gaussians, and an error function step at the ionization potential. Table 2 contains the positions and origin of the individual contributions, whose sum is given by the red line.
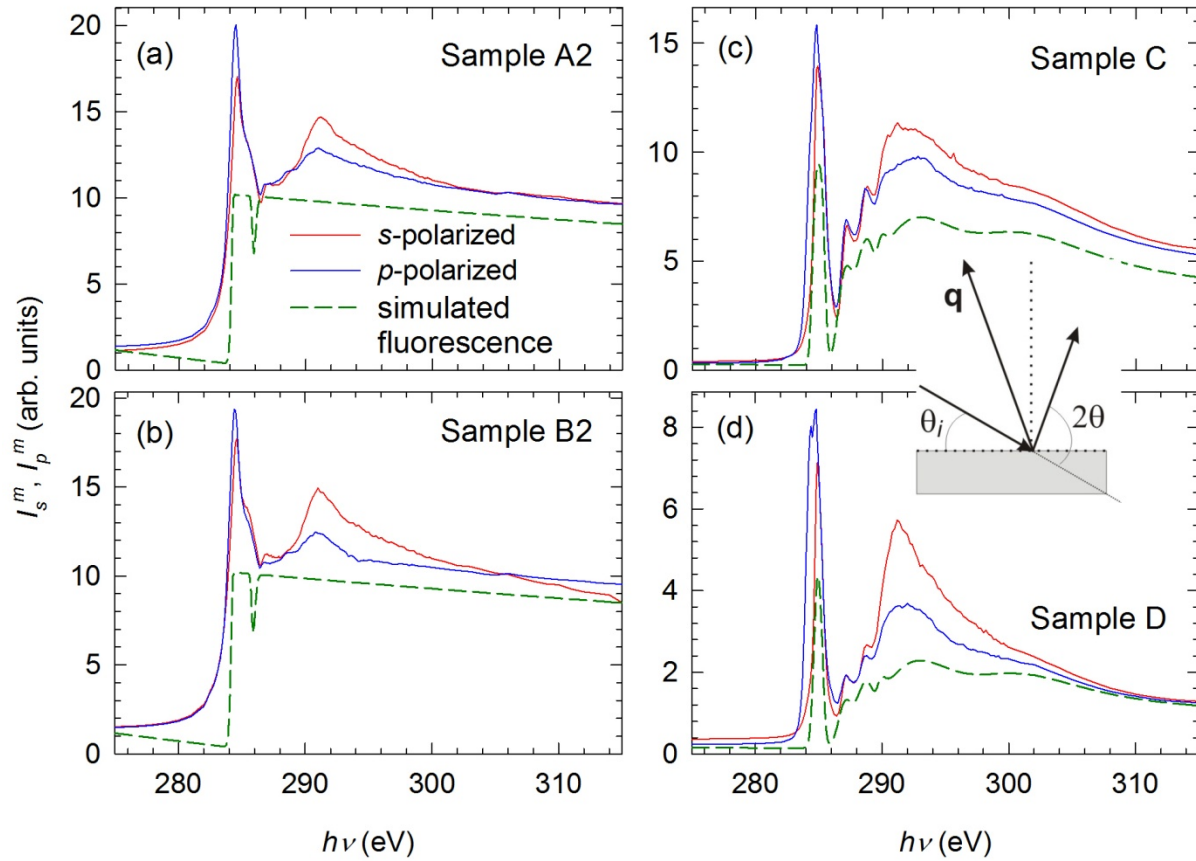
Figure 6. (Color online) High-angle diffuse scattering spectra from 4 different polystyrene samples indicated measured with incident *s*- and *p*-polarization are given by red and blue solid lines, respectively. Inset shows diffuse scattering geometry; for these data $\theta_i = 30°$, $2\theta = 100°$, and $|\mathbf{q}| \cong 2.2 \; nm^{-1}$. Dashed green lines are approximate fluorescence intensities calculated from experimentally determined absorption spectra as described in the text and Supplemental Material [44].
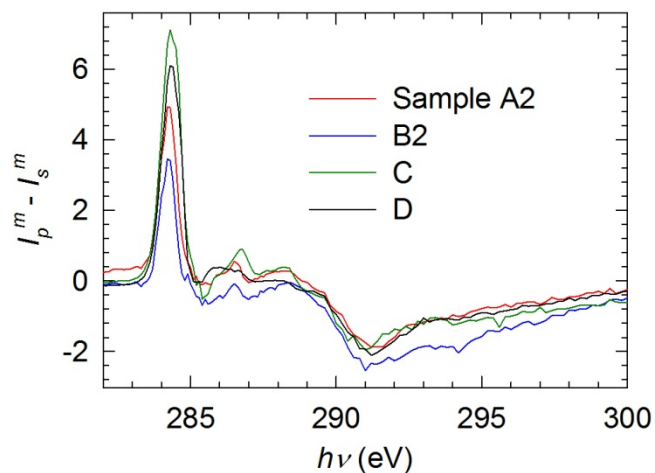
Figure 7. (Color online) The high-angle diffuse anisotropy, $\Delta I^m = I_p^m - I_s^m$, is plotted for each sample from the data in Figure 6. Systematic resonant peaks appear for all samples; most prominent are positive and negative anisotropy associated with phenyl $\pi1^*$ and backbone $\sigma1^*$ features, respectively. Possible experimental artifacts are evident as slow intensity drifts.

Molecular anisotropy effects in carbon *K*-edge scattering: depolarized diffuse scattering and optical anisotropy

Kevin H. Stone[†] and Jeffrey B. Kortright

Materials Sciences Division, Lawrence Berkeley National Laboratory, 1 Cyclotron Road, Berkeley, California 94720, USA

[†]*Current address, Stanford Synchrotron Radiation Laboratory, SLAC National Accelerator Laboratory, 2575 Sand Hill Road, Menlo Park, California, 94025, USA*

This Supplemental Material includes calculations of the spectral dependence of the skin depth and fluorescence yield across the carbon *K*-edge.

Skin depth evaluation
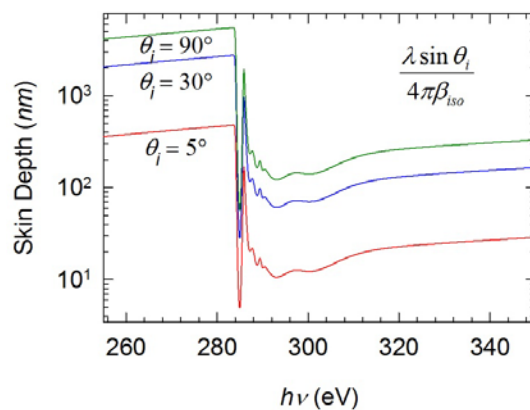
The skin depth for x-ray intensity at 3 incidence angles noted is evaluated using the expression given, where β_{iso} is the isotropic absorption index obtained from $f_{2,iso}$.

Fluorescence yield evaluation

To evaluate the expected fluorescence yield (FY) spectra from the different samples we assume that $f_{2,iso}$ describes absorption, and that fluorescence is emitted at constant $h\nu_{FY}$ and so is absorbed on exit at a rate independent of the incident $h\nu$. The absorption correction, A_{iso}^{FY}, obtained by integrating the incident field intensity at a given depth over the sample, scales the absorption to give the calculated $FY_{iso} \propto A_{iso}^{FY} f_{2,iso}$ as in the figure below for 3 relevant t values. These 3 fluorescence spectra are re-plotted in Figure 6 of the manuscript where they have been scaled by constant values. The same scale factor is used for the thick samples A2 and B2, while a 30% smaller scale factor is used for the ultrathin film samples C and D. The need for different scale factors suggests that the estimated t values of C and D in Table 1 are somewhat greater than their actual values.

It is reasonable to use $f_{2,iso}$ to evaluate the FY from incident s- and p-polarization, rather than separately evaluating $FY_{s/p}$, for the following reasons. The maximum $\Delta\langle f_2\rangle / f_{2,iso}$ is small (10%) at the $\pi1^*$ line, and much smaller elsewhere. Saturation effects in A_{iso} are strongest at the $\pi1^*$ line and thus suppress $\langle f_2\rangle_s$ and $\langle f_2\rangle_p$, and hence their already small difference, most rapidly with t at this line. Any residual $\Delta FY = FY_p - FY_s$ would have a negative sign at the $\pi1^*$ peak and cannot explain the observed positive anisotropy in ΔI^m in Figure 7.